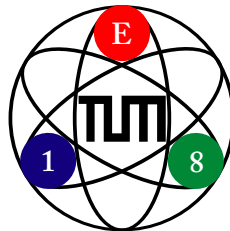**Bachelor Thesis**

Analysis of the $\eta'\pi$ and $\eta\pi$ Final States in COMPASS Data

Christoph Raab

September 14, 2011

Physik Department E18
Technische Universität München

Contents

Chapter 1

Introduction

This Bachelor's thesis describes for a large part the successful crosscheck of the selection of the $\eta\pi$ and $\eta'\pi$ final states by Tobias Schlüter that I performed from April 2011 up to early June 2011. As a result of this work, the analysis of Tobias Schlüter could be presented at the Hadron2011 conference in Munich. A similar analysis/crosscheck had already been performed by Tobias Schlüter and Hauke Wöhrmann.

Theory has long predicted the existence of so-called exotic mesons which go beyond the conventional $q\bar{q}$ model. Their establishment and study is a subject of continued interest in the hadron physics community. One candidate for such an exotic meson is the $\pi_1(1600)$, and one experiment with the versatility and precision to provide significant analyses in the field of meson spectroscopy is COMPASS. The crosschecked event selection has the goal of isolating a specific state with as little background and as many represantatives as possible. To this end, the selection criteria applied to a very large sample of events, the COMPASS 2008 hadron run, grow from general requirements on the quality of the event to the identification of a specific decay chain.

Chapter 2

The COMPASS experiment

2.1 Purpose

The COMPASS (COmmon Muon and Proton Apparatus for Structure and Spectroscoy) experiment is a fixed-target experiment at the CERN North Area. Historically, it was created as a merger of two seperate proposals (HMC and Cheops) and thus serves a broad scientific programme and involves scientists of many institutions. The following section will describe the experimental setup that was used taking the data that are analysed in this thesis, which is the hadron beam setup from 2008.

2.2 Design

The COMPASS experiment is positioned at the end of the M2 beamline fed by the Super Proton Synchrotron (SPS). As illustrated in figure 2.4, the proton beam is directed into a Beryllium production target. This produces predominantly pions, secondary protons and a certain percentage of kaons. The M2 beamline guides the beam from the underground level of SPS to the surface level of COMPASS. The two bending magnets used for this also act as a momentum filter. The length of the beamline allows for the formation of a tertiary muon beam from the decay $\pi \to \mu\nu_\mu$, which can then be selected by the afforementioned bending magnets. As shown in figure 2.3, ČErenkov Differential counters with Acromatic Ring focus (CEDARs) are set in place to identify the various beam particles. Other detectors placed upstream from the target are several trigger detectors and the silicon telescope, which measures the beam direction. The target itself is a barrel of liquid H_2. It is surrounded by a Recoil Proton Detector (RPD) which consists of two rings. The inner ring A is 500 mm long and segmented into 12 slats of scintillating polyvinyl toluoene (PVT) with a PMT (photo-multiplying tube) at each end, the outer ring B is longer (1150 mm) and split into 24 slats. Please see the figure 2.2 for an illustration. This design results in an azimuthal angular resolution of $\frac{\pi}{12}$ by coinciding a slat in the inner ring with either one of the three slats in ring B which are facing it. This scheme is shown in the cross section of figure 2.2, as well. The 655 mm radial separation of the between the rings allows for a measurement of the proton velocity via its time of flight.

The subsequent spectrometer consists of two stages, each with a spectrometer magnet SM1/2, tracking detectors and hadronic and electromagnetic calorimetry (HCAL1/2,

ECAL1/2). The two stages correspond to large and small angles and approximately to low and high energies, as well. This is shown in the figure 2.1. The absorbing components of the first stage have a rectangular hole in their middle in order so that particles can reach the second stage. The larger distance of the second stage from the target gives a better angular resolution at small angles, which is critical in order to separate photons in order to reconstruct particles decaying into photon pairs.
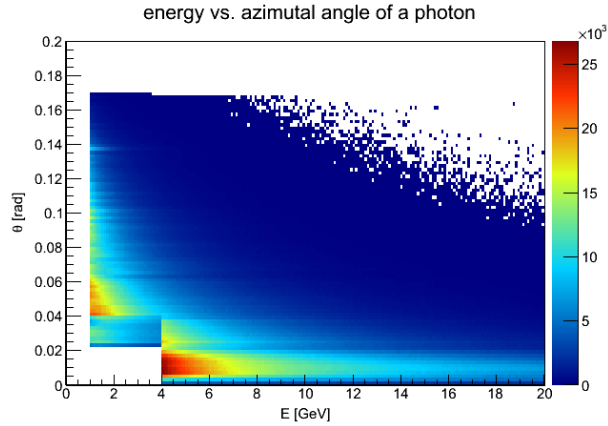

Fig. 2.1: The photon angle with regard to the z axis of the lab system versus its energy deposited in ECAL1 or ECAL2. This plot shows the distinction between high energy/low angle and low energy/large angle components.
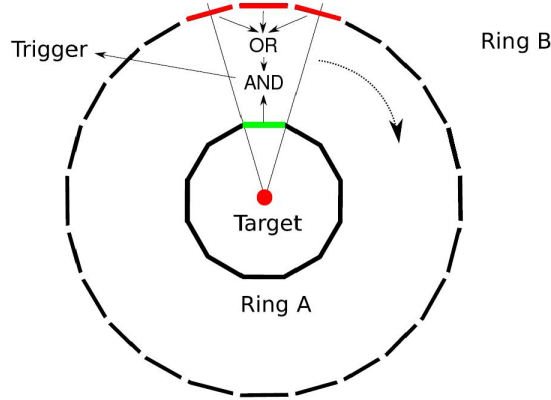

Fig. 2.2: The RPD in a cross section (not to scale). The segmentation and trigger scheme is shown.
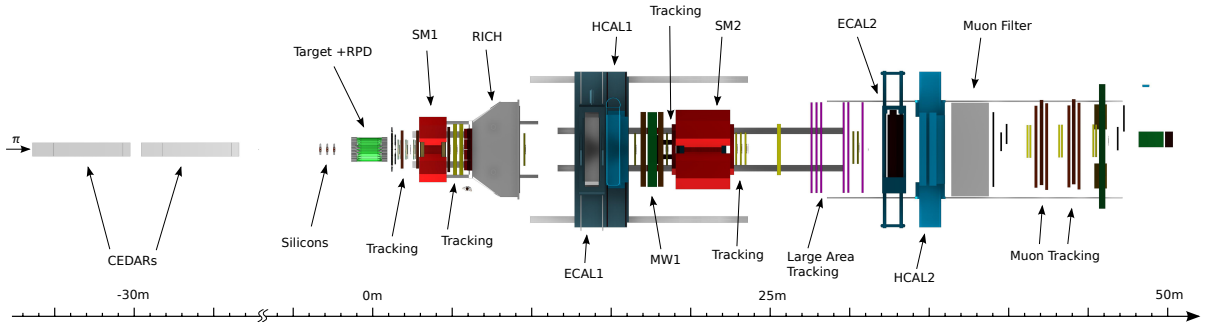
Fig. 2.3: A full top view of the COMPASS spectrometer in its setup from 2008. Image courtesy of Prometeusz Jasinski
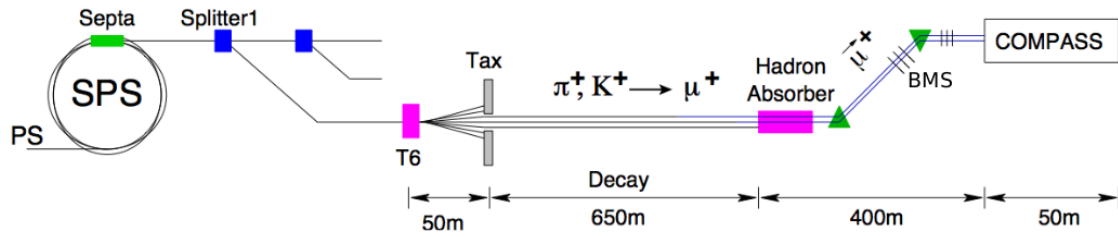.

Fig. 2.4: The M2 beamline, courtesy of M. Leberig [**?**].

2.3 Technical aspects of analysis

This section describes the actual process by which meson spectroscopy is performed at COMPASS. The data format common to each step is the ROOT tree, a data structure that is used to record a set of information for several individual events.

The data flow starts with signals from the various types of detectors described above. These are digitized, collected for each event and written into files called DSTs ("Data Storage Tapes"). These DSTs are processed by a reconstruction software called CORAL. CORAL turns hits in tracking detectors into particle tracks and assigns them a momentum, calorimeter showers into clusters and assigns them an energy, and calculates many other useful pieces of information. The output of CORAL is a so-called *production* in the form of m(ini)DSTs. These mDSTs contain the event information in the form of C++ classes so that they can be used to select events based on physical criteria. This is achieved with a framework called PHAST (PHysics Analysis Software Tools). PHAST can be put to use filtering data with a "user event function", which is a C++ function using classes provided by PHAST to analyse events. Depending on selection criteria applied in a user event function, PHAST can write files containing whole events (so-called μDSTs) or histograms and ROOT trees filled in that user event function. ROOT trees containing kinematical data of a selected sample of events are then entered into

partial-wave analysis. Using a detailed model of the detector, Monte Carlo simulation provides acceptance correction.

The analysis presented in this thesis focuses on the step of event selection; reconstruction and partial-wave analysis are beyond the scope of the limited time available for a bachelor's thesis.

2.4 Motivation

This section describes the physical background of the analysis, the underlying assumptions about the described events as well as a motivation.

In the constituent quark model, a meson is a fermion-antifermion bound system consisting of a quark and antiquark. The quark/antiquark couple to a spin $S = 0, 1$ and can carry an orbital angular momentum L between them. These two in turn couple to the total spin $J = |L - S|, \ldots, L + S$. Commonly used parities are: the parity P which describes the eigenvalue of a state under the parity transformation, and which is conserved by the strong interaction; the C parity, which belongs to charge conjugation but strictly speaking only has neutral particles as eigenstates; and the G parity, which is defined as the C parity times a rotation around the y-axis in isospin space and is well-defined for all mesons. In conventional terms, the C parity of a charged meson is understood as that of its neutral isospin partner. Using basic properties of fermionic systems and the $q\bar{q}$ assumption, these parities can be calculated as

$$P = (-1)^{L+1} \tag{2.1}$$

$$C = (-1)^{L+S} \tag{2.2}$$

$$G = (-1)^I C = (-1)^{L+S+I} \tag{2.3}$$

These equations lead to a set of forbidden quantum numbers not attainable in the constituent quark model, namely the sequence $J^{PC} = 0^{--}, 0^{+-}, 1^{-+}, 2^{+-}, \ldots$

Quantum chromodynamics (QCD), the fundamental theory of the strong interaction, predicts the existence of so-called exotic mesons beyond the constituent quark model. Showing the existence of these exotic mesons is a major goal in hadron physics. Due to their exotic nature, their quantum numbers J^{PC} are not restricted by the above equations. Thus, the preferred method of exotic meson searches is to show the existence of "spin exotics" with J^{PC} quantum numbers impossible for $p\bar{q}$ mesons.

The $\pi_1(1600)$ is a candidate for such an exotic meson. It has been predicted by lattice QCD simulations as a hybrid meson with a mass below $2\,\mathrm{GeV}/c^2$[1]. Since, a number of experiments claim a discovery of the $\pi_1(1600)$ with the spin-exotic quantum numbers $J^{PC} = 1^{-+}$ using various production mechanisms and decay modes. However, along with these individual analyses the state of establishment of the $\pi_1(1600)$ as a resonance remains controversial. The COMPASS experiment provides new opportunities in this regard with its capability of analysing many different decay modes.

Chapter 3

The $\eta'\pi$ and $\eta\pi$ final states

3.1 Properties and decay

After scattering on a proton, the beam particle diffracts into a state X while the proton stays intact. X decays into a final state at the "primary vertex". The two final states chosen for this analysis are $\eta\pi^-$ and $\eta'\pi^-$. In other words, events need to be selected which fit the reaction

$$\pi^- + p \rightarrow X^- + p \rightarrow \eta^{(')}\pi^- + p \tag{3.1}$$

To this end, the decays of these final states need to be reconstructed. The decay occurs in a cascade of intermediate states, resulting in a system of particles which can be considered stable in the context of this experiment. In order to establish this distinction, we calculate the distance a particle might travel before it decays. This distance of course depends on the velocities β and life times τ of the involved particles, or alternatively their energies, masses and decay widths.

$$d = \gamma\beta c\tau = \sqrt{\left(\frac{E}{m}\right)^2 - 1} \cdot \frac{\hbar c}{\Gamma} \tag{3.2}$$

Relativistic time dilatation enters in the form of the factor γ. With the beam energy of $E = 191\,\text{GeV}$ as the largest possible energy and the width of the π^0 of $\Gamma = 7.8\,\text{eV}/c^2$ as the smallest decay width of an intermediate particle involved in the interesting events, the estimated separation between the start and finish of the decay cascade is $d = 35.5\,\mu\text{m}$. As this distance is far below the resolution achievable at the current state of detector technology, the interaction and each occurring decay is assumed to occur instantaneously, in a single point, henceforth called the primary vertex.

The particles in the stable states are $\pi^\pm$ and photons. The $\pi^\pm$ only decay via the weak interaction, giving them a considerable smaller decay width of $2.5 \cdot 10^{-8}\,\text{eV}/c^2$. Using the lower end of the $E(\pi^\pm)$ spectrum of $2\,\text{GeV}$ as a low estimate of the involved energy, the same calculation arrives at a decay length of $d = 112\,\text{m}$. This is longer than the spectrometer itself, which ends $51\,\text{m}$ from the target. The vast majority of $\pi^\pm$ either do not decay in the spectrometer, the small fraction that does travels a long enough distance so that the reconstruction of their trajectory is not inhibited.Free photons are stable unless they convert in an electric field, such as that of a nucleus. Keeping this

in mind, we follow the decay chains of the chosen final states until we arrive at a state consisting only of charged pions and photons.

The goal of the event selection is to attain a large, clean sample of events containing the final state under study. This is done by reconstructing decay channels of the final state; these decay channels need to be chosen. To this end, the branching ratios of the involved decays and the detector efficiencies in reconstructing the resulting system have to be considered. The branching ratios are listed in table 3.1. The reconstruction of events with too many photons is problematic due to their low reconstruction efficiency (compared to charged particles) and combinatorial problems.

Decay	Branching Ratio
$\boldsymbol{\eta'(958)}$: $m = 957.8\,\text{MeV}/c^2$, $\Gamma = 0.19\,\text{MeV}/c^2$	
$\rightarrow \boldsymbol{\pi^+\pi^-\eta}$	**43.2%**
$\rightarrow \rho^0\gamma$	29.3%
$\rightarrow \pi^0\pi^0\eta$	22.7%
$\boldsymbol{\eta}$: $m = 547.8\,\text{MeV}/c^2$, $\Gamma = 1.3\,\text{keV}/c^2$	
$\rightarrow \boldsymbol{\gamma\gamma}$	**39.3%**
$\rightarrow 3\pi^0$	32.5%
$\rightarrow \boldsymbol{\pi^+\pi^-\pi^0}$	**22.7%**
$\boldsymbol{\pi^0}$: $m = 134.9\,\text{MeV}/c^2$, $\Gamma = 7.8\,\text{eV}/c^2$	
$\rightarrow \boldsymbol{\gamma\gamma}$	**98.8%**
$\boldsymbol{\rho(770)^0}$: $m = 775.5\,\text{MeV}/c^2$, $\Gamma = 149\,\text{MeV}/c^2$	
$\rightarrow \pi^+\pi^-$	100%

Table 3.1: Intermediate particles with branching ratios of their most common decays ($> 10\%$). The ones actually involved in the selection are marked in bold.

Of the η' decays, the $\pi^0\pi^0\eta$ results in at least six photons and is excluded due to this number. The $\rho^0\gamma$ decay results in one photon and two charged pions. This case is still a possiblity for future analysis, but was not preliminarily chosen due to the comparatively large background of the $\rho(770)$ itself and background events from $\gamma\gamma$ decays where one photon was not detected. Each η' in this analysis is reconstructed from a decay to $\pi^+\pi^-\eta$.

The η has a handily large branching ratio for the simple $\gamma\gamma$ decay. The $3\pi^0$ decay results in a hard to handle number of photons. The other practical channel is to reconstruct the decay to $\pi^+\pi^-\pi^0$.

The π^0 decays predominantly to $\gamma\gamma$, which is why this decay was used to reconstruct each π^0.

In theory, this gives us two channels for $\eta'\pi$ and two for $\eta\pi$. In praxis, the channel where $\eta\pi^- \rightarrow \gamma\gamma\pi^-$ is disregarded. This is due to two problems: For once, with only one charged particle, the reconstruction of the primary vertex (see earlier this section) is more difficult. But most important, this selection would include a background of elastically scattered events. Unless these events were otherwise differentiated, the resulting sample

would have lower quality. Note that the BNL experiment E852 used this very channel in their analysis of the $\eta\pi^-$ final state [2].

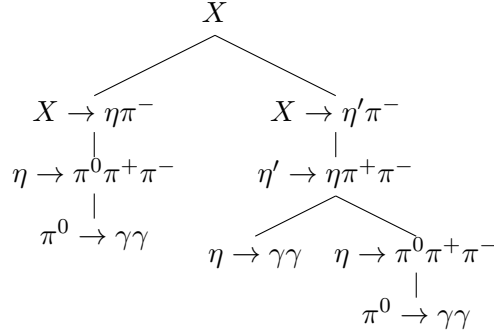In conclusion, the following decay chains are analysed:

$$X$$

$$X \to \eta\pi^- \qquad\qquad X \to \eta'\pi^-$$

$$\eta \to \pi^0\pi^+\pi^- \qquad\qquad \eta' \to \eta\pi^+\pi^-$$

$$\pi^0 \to \gamma\gamma$$

$$\eta \to \gamma\gamma \quad \eta \to \pi^0\pi^+\pi^-$$

$$\pi^0 \to \gamma\gamma$$

Fig. 3.1: Summary of the analysed decay chains.

3.2 Methods

Kinematic fitting

A *constrained fit* is a mathematical operation on a multi-dimensional fit parameter y^a. Its objectiv is to find a variation e^a so that it satisfies a constraint:

$$F(y^a + e^a) = 0 \tag{3.3}$$

The variation e^a is chosen so that the the error χ^2 measured in the multi-dimensional parameter space is minimal. To this end, a metric has to be introduced:

$$\chi^2 = e^a C_{ab}^{-1}(y^a) e^b \tag{3.4}$$

Mathematically, C is called the coveriance matrix. Its non-diagonal elements imply a correlation between the parameters. This type of problem can be solved with standard methods such as Lagrangian multiplicators. A kinematic fit such as the one applied in this analysis is a type of constrained fit. Its constraint takes the form of

$$p_\mu p^\mu - m_0^2 = 0 \tag{3.5}$$

That is, a four-momentum vector depending on fit parameters $p^\mu(y^a)$ has a certain invariant mass m_0. This can be motivated by the following application:

The η decays into two photons, which interact in the electromagnetic calorimeters of COMPASS and create two calorimeter showers, which are reconstructed as clusters with energies $E_{1,2}$ and positions $\vec{x}_{1,2}$. From these values, the four-momenta of the responsible photons can be reconstructed. Photons are massless and carry no charge. Assuming a photon being emitted at the primary vertex and depositing its whole energy in the

calorimeter, the four-momentum of the photon can be simply composed of the energy recorded in the calorimeter cluster, scaled by a calibration factor, and the three-vector with the direction connecting the PV of the event to the location of the cluster and the energy as its magnitude. The four-momenta of two photons reconstructed in this fashion can then be added, the resulting invariant mass of two photons with the energies $E_{1,2}$, with an angle θ between their momenta is then

$$m(\gamma\gamma) = 2E_1E_2(1 - \cos\theta) \tag{3.6}$$

The energy resolution of the electromagnetic calorimeters is [7]

$$\frac{\sigma(E)}{E} = \frac{5.5\%}{\sqrt{E}} \oplus 1.5\% \tag{3.7}$$

This energy resolution visibly spreads out the η peak in the digamma mass spectrum to a Gaussian with a width on the order of $21\,\mathrm{MeV}/c^2$. The resonance itself however only has a width of $\approx 1.3\,\mathrm{keV}/c^2$. Therefore, a kinematic fit of the photon pair to η (meaning, with the constraint $m(p_{\gamma_1} + p_{\gamma_2}) = m(\pi^0)$) seems justified. That the resulting effect is in fact a correction of the error in the measured energy can be seen in the plot showing the before and after in the $\pi^+\pi^-\gamma\gamma$ spectrum 3.3 and the same mass versus the mass of the contained $\gamma\gamma$ 3.2.
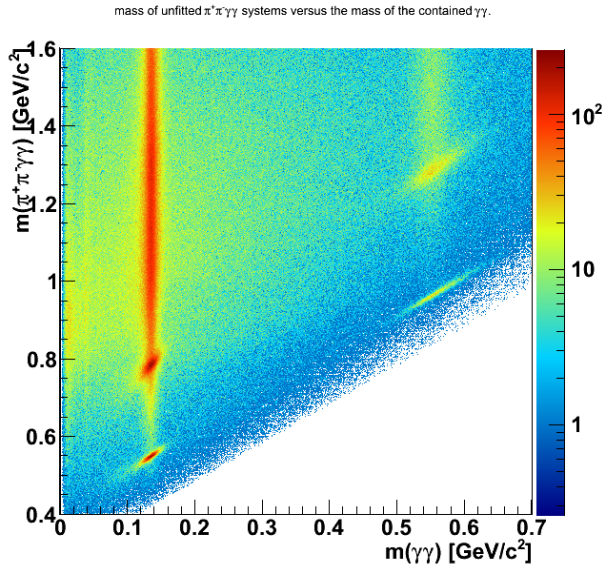

Fig. 3.2: The $\gamma\gamma$ mass versus the the mass of the $\pi^+\pi^-\gamma\gamma$ system containing it for three charged pions. This plot clearly shows that the variances of the peaks in the $\pi^+\pi^-\gamma\gamma$ mass spectrum are mainly due to the widths of the peaks in the $\gamma\gamma$ spectrum. The decays of $\eta \to \pi^+\pi^-\pi^0$ and $\eta' \to \pi^+\pi^-\eta$ are clearly visible alongside the more diffuse $\omega(782)$ and $f_1(1285)$.
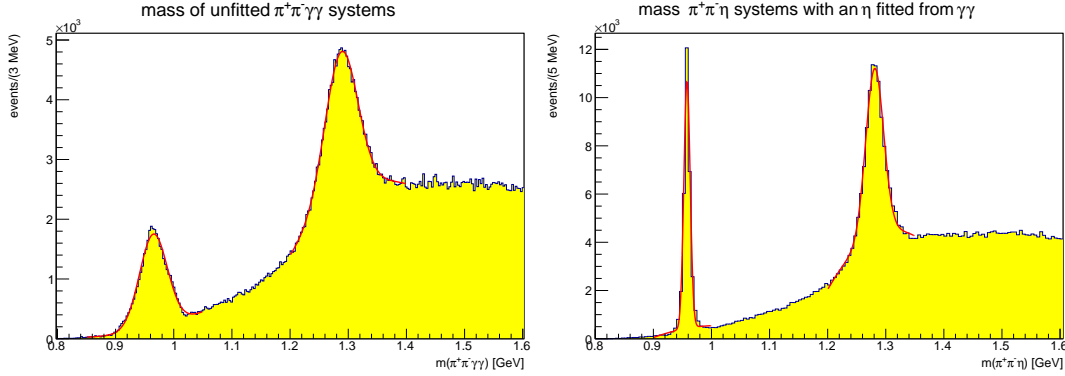
Fig. 3.3: For events with three charged pions, the effect of the kinematic fit of two pho-
tons to the η mass is shown on the $\pi^+\pi^-\gamma\gamma$ spectrum. The kinematic fit
significantly reduces the widths of both visible peaks belonging to the $\eta'(985)$
and $f_1(1285)$. The results of the kinematic fit are listed in 3.2

Peak mass, width $[\,\mathrm{MeV}/c^2\,]$	$\eta'(958)$	$f_1(1285)$
without kinematic fit	$m = 964.9,\ \Gamma = 23.6$	$m = 1287.9,\ \Gamma = 28.0$
with kinematic fit $\gamma\gamma$ to η	$m = 957.9,\ \Gamma = 5.4$	$m = 1280.8,\ \Gamma = 16.1$
PDG mass, partial width	$m = 957.8,\ \Gamma = 0.08$	$m = 1281.8,\ \Gamma = 12.6$

Table 3.2: Results of the fit of the plots in 3.3. The peaks were fitted as Gaussians on
top of a linear background. The standard derivation is given as the width of
the peak. The PDG widths are the partial widths for the relevant decays.
Both peak positions are brought closer to the PDG masses, and both become
narrower.

Such a kinematic fit was developed by Tobias Schlüter and described in a COMPASS
note [4]. It features prominently in this analysis in three incarnations. All three have in
common that two calorimeter clusters are the only fit parameters involved. They differ
in their constraint. The simplest form is a constraint on the digamma mass, like in the
example above; it finds use in each of the chosen decay channels. Another one fits a sum
of four-momenta including two photons to a mass, and is applied in the two channels
with three charged particles for both the $\eta\pi^-$ in section 3.4.1, and $\eta'\pi^-$ in section 3.4.2.
The last one applies two constraints, one for the digamma mass and another one for the
invariant mass of a sum of four-momenta including two photons, and is applied as the
last step of the channel where $\eta'\pi^{\to}5\pi^{\pm}\pi^0$ 3.4.3.

Cluster calibration

The calorimeter cells in the electromagnetic calorimeters in COMPASS exhibit re-
sponses to photons which differ among them in their magnitude for the same energy of
a photon. The function deriving the energy of the photon which caused a calorimeter

shower from the signals of the cells involved in that shower therefore needs to contain a scaling factor for the energy deposited in each cell. That is

$$E_{\text{calibrated}} = \text{scaling(cell)} \cdot E_{\text{uncalibrated}} \tag{3.8}$$

In the data from production slot 3 available for this analysis, the π^0 peak in the digamma mass spectrum exhibited an offset from the PDG π^0 mass, indicating a systematic error in the current calibration. A preliminary calibration to mitigate this error was developed by Tobias Schlüter [5].

The method proceeds this way:

1. A large sample of data is obtained where two calorimeter clusters have been measured, and the resulting digamma mass lies within a window around the π^0 mass.

2. Then, a kinematic fit (see the previous section 3.2) is performed to transform the energies of these clusters.

3. The change in each cluster energy is then considered a scaling factor for the central cell or cells of the clusters and averaged over the sample of events.

4. Using the already-obtained scaling factors, the process is then iterated.

In the production slot 4, a more advanced calibration which is currently being developed by Sergei Gerassimov will be implemented, where the scaling factor can depend on the cluster energy and time, as well.

3.3 Preselection

The cross-checked selection of the final states was performed in two stages. The first stage (section 3.3.1) was a pre-selection, part of a combined skim of the 2008 hadron mDSTs and used only basic cuts, trying to ensure clean, mostly exclusive events. The channel-specific selection was limited to the number of neutral clusters and charged tracks in the outgoing system. Its goal was to reduce the data to a manageable amount, producing so-called μDSTs. The second stage started with another preselection (section 3.3.2) which used said μDSTs as input and involved tighter and more advanced exclusivity cuts and kinematic fits. It then continued with the final selection (section 3.4), which identified the required final states. Its end product were the trees entering into partial-wave analysis.

3.3.1 Preselection, first stage

DT0 trigger

The DT0 trigger is logically composed as aBT and RPD and not Veto, where aBT is the alternative Beam Trigger, RPD the proton trigger and Veto a further composed signal delivered by the veto system of COMPASS. Its purpose is to select an interaction between a beam particle and a target proton with a diffractively produced intermediary

state which decays inside the spectrometer's acceptance, and it is commonly used in the COMPASS 2008 hadron programme.

In principle, it would be reasonable to require that the beam particle should be a π^- and not part of the 2.4% of K^- in the beam. This percentage could be reduced in the selection to some degree by using the CEDAR particle identification detectors. As their behaviour is however not yet fully described in CORAL, this step was omitted.

Best primary vertex

The primary vertex (see section 3.1) is reconstructed as the the closest point of approach of the extrapolated beam and outgoing particle trajectories. The *best* primary vertex is such a vertex that contains the highest number of exiting particle tracks.

At this stage, 14% of events contain no primary vertex, 80% contain exactly one and only 5% contain more than one. As the best primary vertex is likely to be the physical one, discounting 5% of events without further consideration does not seem justified.

Target cut

For the radius r and z coordinate of the primary vertex in the cylindrical lab system, it is demanded that

- $-75\,\mathrm{cm} \leq z(PV) \leq -25\,\mathrm{cm}$

- $r(PV) \leq 2.0\,\mathrm{cm}$

A desired physical event describes the interaction of a beam pion inside the target material. On the other hand, all the material surrounding the liquid hydrogen of the target (the target container walls, parts of the spectrometer) can also give rise to an interaction producing several charged particles. The point of interaction is within reasonable error the primary vertex (see 3.1), therefore the radial and z coordinates of the PV are suitable to cut on the dimensions of cylindrical target container. In this step, the cuts are deliberately broad. They are tightened in the second stage of the selection in section 3.3.2.

Number of charged particles

Since the intended selection includes either 3 or 5 charged pions, the number of charged particle tracks from the primary vertex is required to be $\in \{3, 4, 5\}$. The case of 4 charged pions is excluded implicitly by the cut on the charge sum (see below).

Charge conservation

Assuming an elastic scattering $\pi^- + p \rightarrow X^- + p$ and subsequent decay of X^- into the outgoing system, the charge is conserved as the charge of the beam particle. Here, it is calculated as the sum of the charges of the charged particles exiting the primary vertex. Assuming correct charge values for the individual particles, incorrect sums of the
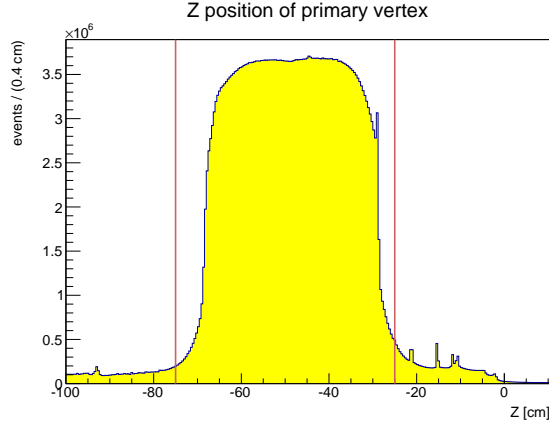
Fig. 3.4: The Z position of the primary vertex. The cut $-75\,\mathrm{cm} \leq Z(PV) \leq -25\,\mathrm{cm}$ applied at this stage is marked and the length of the target is clearly visible within this interval. The Z positions of silicon microstrip detectors within the RPD also appear as sources of primary vertices outside the target length interval.

charges are due to charged particles which were missed by the detector or reconstruction software. Such an event is obviously unfit for analysis. As is discussed in 3.6, for each particle track two methods exist in Phast to obtain the charge of the particle. Events where one gave a correct and the other an incorrect value make up 0.01% of events. In order to ensure a good quality of this simple cut and in light of the minute loss in events, both were required to result in the correct sum, leaving 62% of events considered at this step.

Number of photons

The number of photons in the outgoing system is selected to be $\in \{2, 4, 6\}$. Each photon supposed to hit a calorimeter and create an electromagnetic shower, resulting in a "good" calorimeter cluster. Such a "good" cluster is defined by the following cuts:

- It has no charged particle tracks pointing towards it. This is required as charged particles like $\pi^{\pm}$ or $e^{\pm}$ from the conversion of a photon in a nuclear field $\gamma \to e^+e^-$ also interact in the electromagnetic calorimeters.

- It occurs in either ECAL1 or ECAL2, which are the relevant calorimeters for photons to deposit their energy into.

- It has a time associated with it which, relative to the mean time of the beam particle, obeys $-8\,\mathrm{ns} \leq t_{\mathrm{cluster}} - t_{\mathrm{beam}} \leq 10\,\mathrm{ns}$. In the range of of the z position distributions for clusters and primary vertices, the time for a photon to travel from a primary vertex within the target to an electromagnetic calorimeter can be found to have an estimated variation of $3.5\,\mathrm{ns}$ for ECAL1 and $1.7\,\mathrm{ns}$ for ECAL2. This
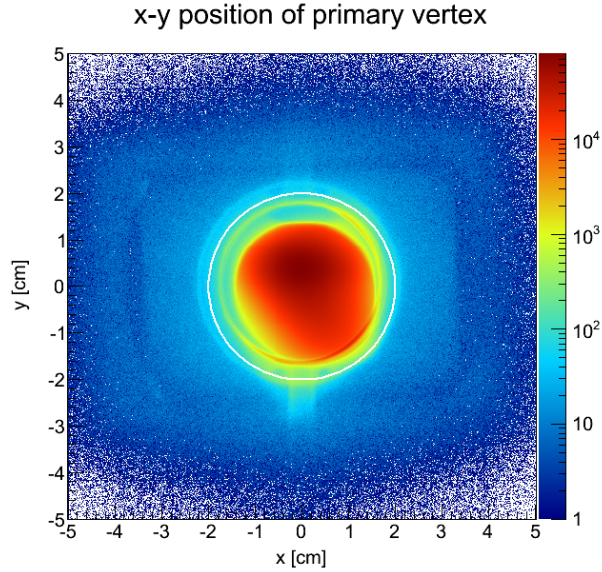
x-y position of primary vertex

Fig. 3.5: The location of primary vertices in the x-y plane, shown in colour on a logarith-
mic scale. The radial target cut is shown in white. Several features are clearly
visible as illuminated by the beam: Moving from the inside out, the inner most
is the target material. The inhomogenous illumination by the pion beam is
visible with a centre at $\approx (0\,\text{cm}, 0.4\,\text{cm})$ and an asymmetric extension to the
lower right, while the level of the liquid hydrogen appears as a depleted area
at the top. The projection of the target container wall is visible as a ring of
radius $\approx 1.5\,\text{cm}$. In addition, hints of the target support structure and silicon
microstrip detectors (see figure 3.4) appear.

variation, together with further errors in the time measurements, contributes to
the width of the main peak in the time spectra in figure 3.6. A cut on this main
peak around $t = 0\,\text{ns}$ is used to reduce pileup events, i.e. events where particles in
the outgoing system are not all the result of the same primary interaction.

- The energy exceeds the lower bounds of $E \geq 1.0$ for ECAL1 and $E \geq 4.0$ for
  ECAL2. These two energy thresholds are supposed to reduce noise introduced
  at low energies; however, the thresholds might still be too high. The various
  combinations of these thresholds are visible in the $m(\gamma\gamma)$ spectrum (figure 3.8).
  They do not seem to ingress into the two relevant peaks.

- In ECAL2, clusters within the cells obsured by the HCAL1 calorimeter are dis-
  carded. This limits their position to $-17 \cdot 3.83\,\text{cm} \leq y_{\text{cluster}} \leq 16 \cdot 3.83\,\text{cm}$, where
  $3.83\,\text{cm}$ is the side length of a cell. The shadow of HCAL1 is treated as an exclusion
  criterium as it was not yet considered in CORAL. In the digamma mass spectrum
  for two photons in the outgoing system, the decays $\pi^0 \to \gamma\gamma$ and $\eta \to \gamma\gamma$ are visible
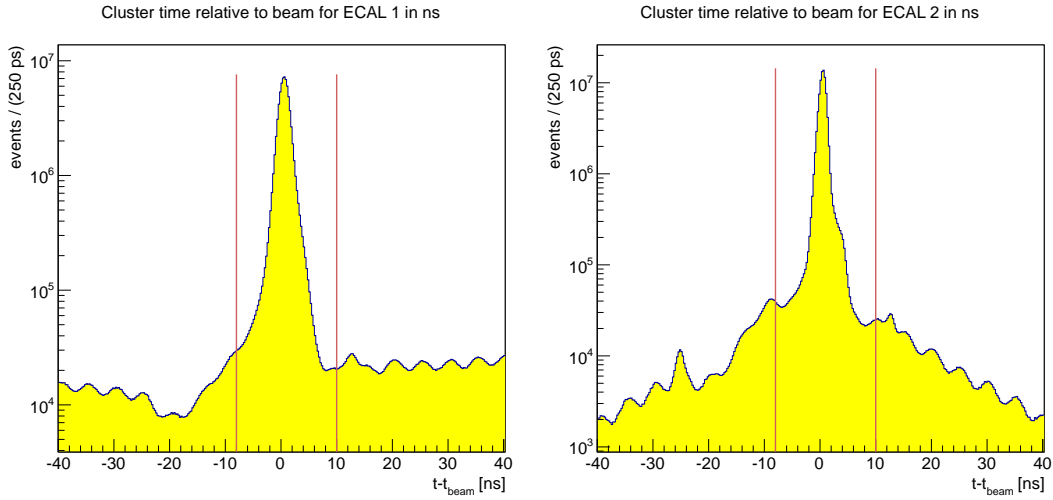 as approximately Gaussian peaks on a background. Their shape is a result of the

Fig. 3.6: The time spectra for calorimeter clusters on a logarithmic scale, on the left for ECAL1 and on the right for ECAL2. The cut made to select "good" clusters is marked.

uncertainty in the measured quantities; the natural partial width of these decays is $7.7\,\text{eV}/c^2$ for the π^0 and $0.51\,\text{keV}/c^2$ for the η, while using a fit to a Gaussian with a linear background, the widths of the peaks can be estimated as $6\,\text{MeV}/c^2$ for the π^0 and $21\,\text{MeV}/c^2$ for the η. Here, the first method of reducing the error in the energy measurement comes into play, namely the calibration described in section 3.2. As can be seen in figure 3.9, both the π^0 and η peaks are improved by the ECAL calibration. Said improvement is characterised mainly as a shift of the peak maxima closer to the PDG masses and also as a reduction of their width.

Energy conservation

Conservation of energy requires that

$$E_{\text{beam}} + E_{\text{target}} = E_X + E_{\text{recoil}} \tag{3.9}$$

If an event is exclusive in the sense that each particle created in the primary interaction is considered in the event selection, this equation will have to hold. As the difference $E_{\text{recoil}} - E_{\text{target}}$ is however typically smaller than $340\,\text{MeV}$ (see figure 3.13), the exclusivity condition is simplified as a cut on the total energy of charged particles and neutral calorimeter clusters, with the calorimeter calibration applied. It is required to be $175\,\text{GeV} \leq E_X \leq 205\,\text{GeV}$. The cut window is chosen to be very wide as the calorimeter energies introduce a large error into the sum. This will later be mitigated by a kinematic fit.
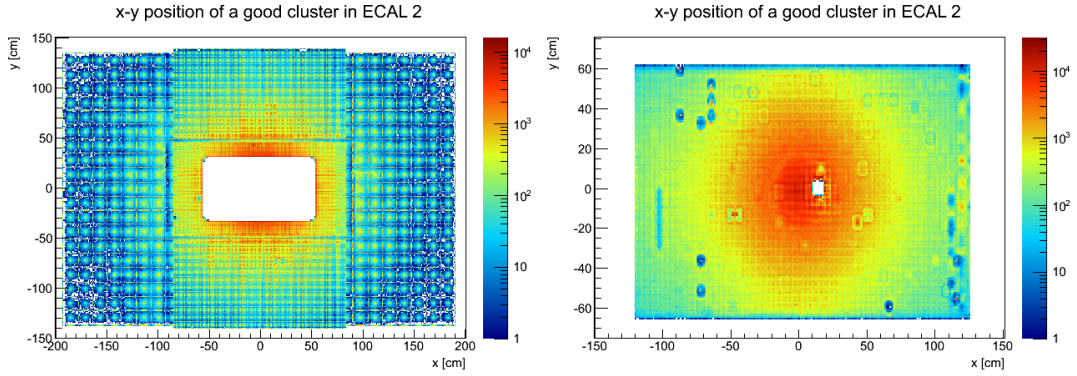
Fig. 3.7: The position of selected photons on the calorimeters ECAL1 (left) and ECAL2 (right), in a logarithmic scale. Both show calorimeters an intensity decreasing outwards and a rasterisation due to their cell structure. In the left figure, the 3 different types of cells present in ECAL1 are clearly visible. Note that on the right, the cut on the shadow of HCAL1 at the top and bottom was already applied. In the right figure, several cells appear with different efficiencies than the surrounding ones. Quite faintly on the logarithmic scale, the shadow of a pipe in the RICH detector appears as a ring with radius $\approx 20\,\text{cm}$.
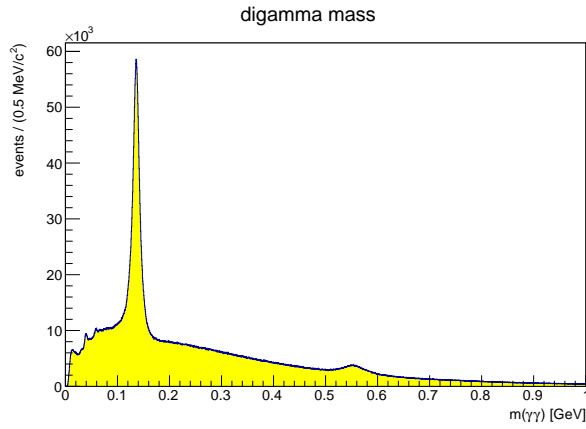
Fig. 3.8: The $m(\gamma\gamma)$ spectrum, with calibrated energies for events containing two good clusters. At the lower end of the mass spectrum, the three distinct combinations of energy thresholds imposed on good clusters from either of the electromagnetic calorimeters are visible. The peak around $135\,\text{MeV}$ corresponds to the π^0, while the decay $\eta \to \gamma\gamma$ is visible around $548\,\text{MeV}$. The η peak has both a larger width and larger background relative to its amplitude.
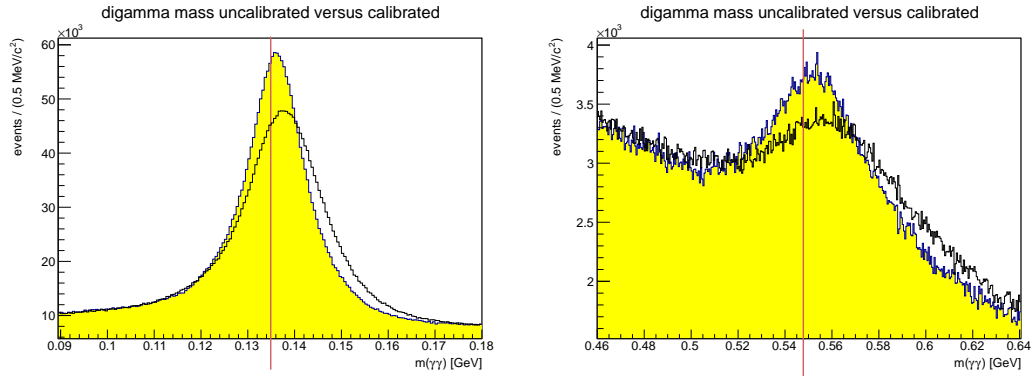
Fig. 3.9: The digamma-mass spectrum before and after the application of the π^0 calibration, with the latter marked in yellow and the PDG masses marked in red. The figure to the left is a close view on the π^0 while the right one shows the η in detail.
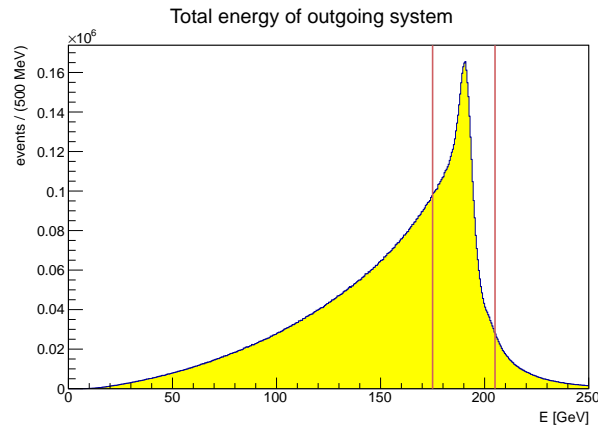

Fig. 3.10: The total energy of the outgoing system with 3 or 5 charged particles and 2, 4 or 6 neutral clusters. The cut applied for exclusivity is marked.
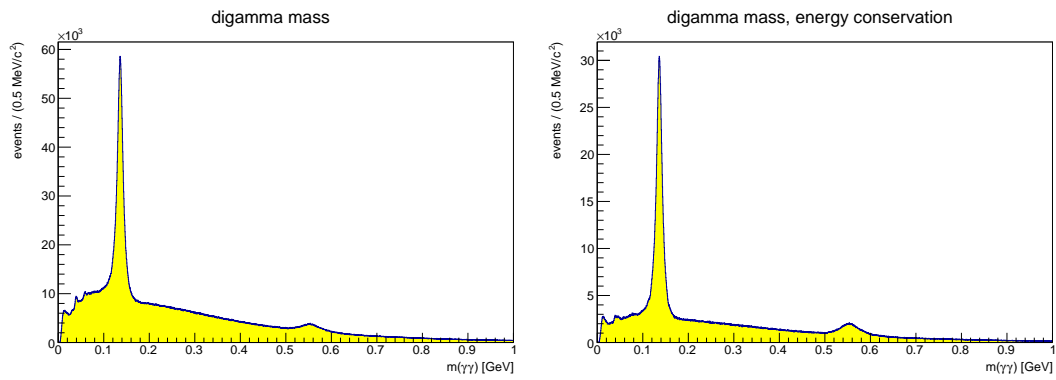
Fig. 3.11: The m($\gamma\gamma$) spectrum before (left) and after (right) the first stage energy cut. The background level relative to the peak amplitude is significantly reduced.
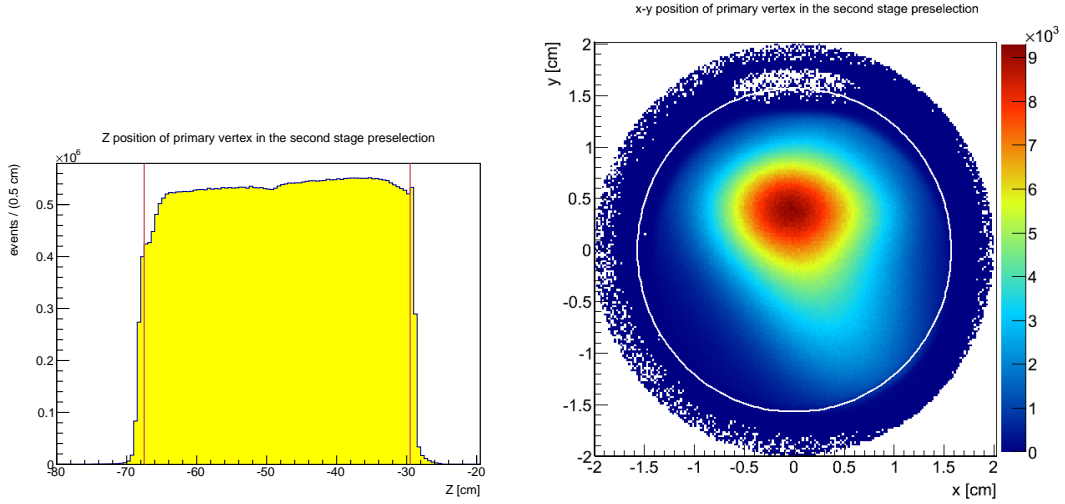
Fig. 3.12: (left) The z position of the primary vertex during the second stage preselection. The target cut interval is marked. Notable differences to the equivalent figure in the first-stage preselection (figure 3.4) are the increased sharpness of the edges of the target interval and the lower background level. (right) The x-y position of the primary vertex in the preselection of the second stage. The final target cut interval is marked. The wall is visibly excluded by the cut.

3.3.2 Preselection, second stage

Number of photons

The number of photons is now a tighter selection of either two or four, and uses the same definition of a good cluster as the first stage of the preselection.

Target cut

- $-67.5\,\mathrm{cm} \leq z(PV) \leq -29.5\,\mathrm{cm}$

- $r(PV) \leq 1.57\,\mathrm{cm}$
  These are the actual dimensions of the cylindrical target container, slightly shrunk in order to exclude the walls. The accompanying plots are shown in the figure 3.12, where the cuts are also marked.

One recoil proton

The assumed elastic scattering leaves a recoil proton, to be detected in the RPD. As the direction of the recoil proton is going to be used later in an exclusivity cut, a single recorded proton track is required. Further, proton tracks appear with a momentum of 0. Because the proton momentum as measured by the RPD is given by the time of flight

between its two shells, a momentum of exactly 0 is impossible; instead, this value is used as a flag for a failed reconstruction.
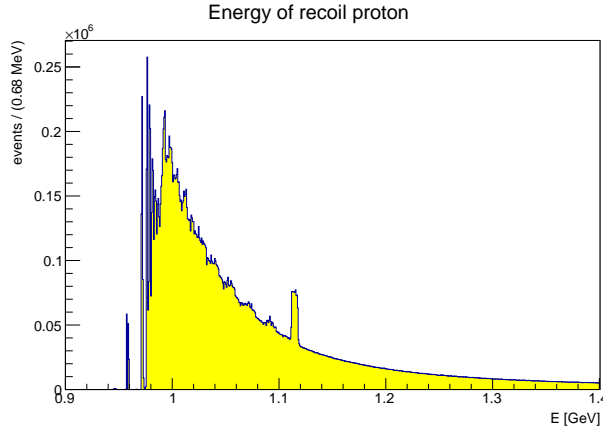

Fig. 3.13: The energy of the recoil proton recorded by the RPD. Going from left to right, after the the start at the proton mass of 938 MeV, peaks at discrete values appear, followed by a continuous spectrum. Physical values start at an energy of 0.97 GeV, corresponding to the minimally accepted proton momentum of 250 MeV. The continous spectrum rapidly decreases at energies higher than ≈ 1 GeV. A discontinuous surplus appears at energies around 1.115 GeV, equivalent to a flight time of 4.0 ns between the RPD's two shells. This structure is likely to be artificial in nature.

Two photons in the outgoing system

Until now, the option had been open to consider channels were two π^0 decay into 4 γ. With the analysis focusing on the $\eta\pi^-$ and $\eta'\pi^-$ final states, only the case of 2γ remains.

Either π^0 or η

As discussed in section 3.3.1, the $\gamma\gamma$ mass spectrum exhibits peaks for the decays of the π^0 and the η. Each of these resonances plays a role in the chosen decay channels, therefore the peaks are selected as either of

- $\left|m(\gamma\gamma) - m(\pi^0)\right| < 20\,\text{MeV}$

- $\left|m(\gamma\gamma) - m(\eta)\right| < 50\,\text{MeV}$

As calculated in section 3.3.1, the partial natural decay widths of these resonances are negligible against the width of their peaks in the digamma mass spectrum. This justifies the application of a kinematic fit of the Lorentz vectors with the mass constraints $m(\gamma\gamma) = m(\pi^0)$ or $m(\gamma\gamma) = m(\eta)$. If this fit is successful, the event is taken as containing the π^0 or η, respectively. An event where the fitted $\gamma\gamma$ pair in fact resulted from an η

or π^0 decay, the error in the photon energy is reduced. This step improves the possible exclusivity cut, as is detailed in the next section.

Exclusivity

To improve the exclusivity of analysed events, two different types of cuts were used. The energy exclusivity cut, detailed in section 3.3.1 is similar to the one performed in the pre-selection. The $\Delta\phi$ exclusivity cut is motivated as an augmentation of the energy exclusivity cut, which is limited due to the variance in the beam energy. The outgoing system for which the exclusivity variables are calculated contains a kinematically fitted photon pair. The correction to the photon energies made by the kinematic fit leads to a narrower exclusivity peak and a spreading of the energies of non-exclusive events, and thus a smaller non-ecxclusive background. $\Delta\phi$ is defined as the angle between the projections of the momenta $\vec{p}_X$ and $\vec{p}_{\text{recoil}}$ transverse to the beam direction. For an illustration see figure 3.14. It is calculated

$$\Delta\phi = \sphericalangle(\vec{p}_X \times \vec{p}_{\text{beam}}, \vec{p}_{\text{RP}} \times \vec{p}_{\text{beam}}) \tag{3.10}$$

The interesting property of $\Delta\phi$ is that it is not kinematically linked to the absolute values of the momenta involved, freeing a cut on $\Delta\phi$ from the beam energy variance. Taking conservation of momentum as the basis of this cut gives

$$\vec{p}_X \cdot \vec{p}_{beam} = (\vec{p}_{\text{beam}} - \vec{p}_{\text{RP}}) \cdot \vec{p}_{\text{beam}} = -\vec{p}_{\text{RP}} \cdot \vec{p}_{\text{beam}} \tag{3.11}$$

Thus, the physically expected value is $\Delta\phi = \pi$, which is the maximum appearing in figure 3.16. The beam direction is measured by the silicon telescope, a series of tracking detectors upstream from the target. The direction of the recoil proton is measured in the RPD using the segmentation of its scintillator barrel. Hence, the resolution of the measurement of $\Delta\phi$ is dominated by the azimuthal angle resolution of the RPD, which is $\frac{\pi}{12}$ given by the segmentation of the RPD's shells (see 2.2).

- The energy of the outgoing system with kinematically fitted $\gamma\gamma$ is limited to the range $186\,\text{GeV} \leq E_X \leq 196\,\text{GeV}$.

- From the above calculation, it is demanded that $\Delta\phi \geq \pi - \frac{\pi}{12} \approx 2.9$.

The figure 3.16 shows the correlation between the two exclusivity cuts; that is, a cut on either of two quantities reduces the non-exclusive background of the other, as well.

3.3.3 Summary

With both stages combined, the preselection reduced the event sample to $7.9 \cdot 10^{-4}$ of its original size. The steps taken to identify single decay channels will again reduce the sample by several orders of magnitude.
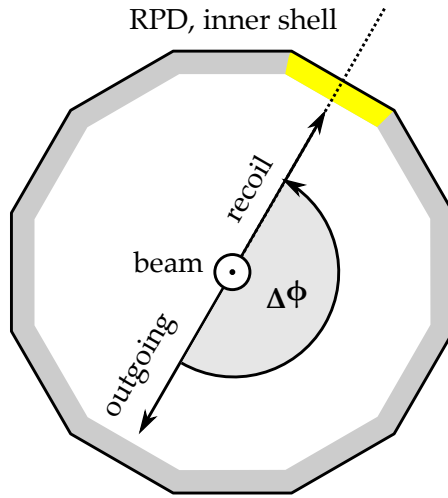
Fig. 3.14: Illustration of the quantity $\Delta\phi$.

Cut	Percentage of events left after the cut
Start	100%
DT0 trigger	75.07%
Best primary vertex	63.65%
Target cut	56.16%
Number of charged particles $\in 3, 4, 5$	15.85%
Charge conservation	9.95%
Number of photons $\in 2, 4, 6$	2.26%
Energy conservation	0.74%

Table 3.3: Cut statistics for the preselection, first stage.

Cut	Percentage of events left after the cut
Start of stage 2	100%
Number of photons $\in 2, 4$	89.7%
Target cut	85.6%
One recoil proton	63.0%
Two photons	39.4%
Two photon kinematic fit	15.1%
Exclusivity	10.7%

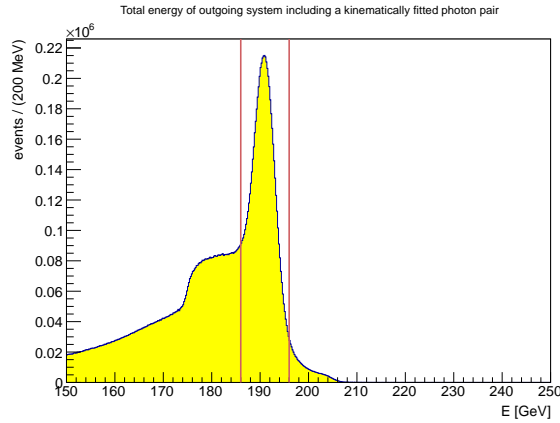Table 3.4: Cut statistics for the preselection, second stage.

Fig. 3.15: The energy of the outgoing system with a kinematically fitted $\gamma\gamma$ pair. The limits set for the exclusivity are marked. By comparing with figure 3.10, the kinematic fit can be seen to have the effect of spreading the energies of background events and leaving the exclusivity peak intact.
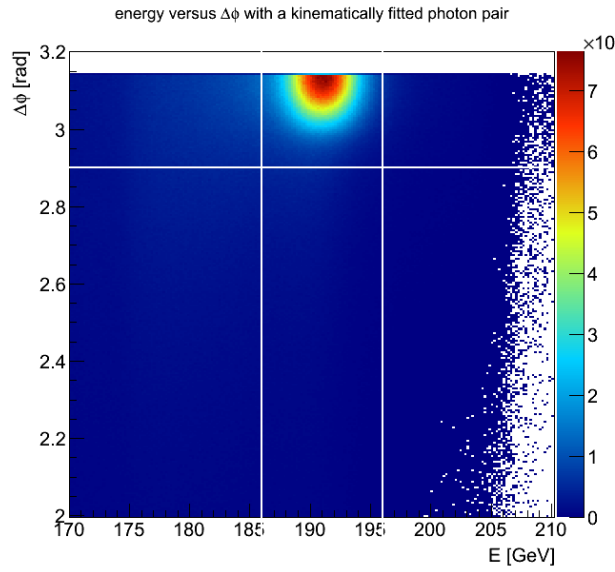

Fig. 3.16: The energy and $\Delta\phi$ used in the exclusivity cut are entered into a 2-dimensional histogram. The cuts applied on both quantities are marked. The correlation between the two cuts is visible.

3.4 Final Selection

3.4.1 Second stage, channel $\eta\pi^- \to (\pi^+\pi^0\pi^-)\pi^-$

The state consists of 2 π^-, 1 π^+ and a π^0 which was fitted from 2 γ clusters. The event is required to contain a π^- so that $\left|m(\pi^+\pi^-\pi^0) - m(\eta)\right| < 20\,\mathrm{MeV}/c^2$, which is considered an η candidate. This is the case for 7.6% of the events that are considered in this channel. At this stage, two combinations (using either of the π^- respectively) are possible, of which just one is chosen. In theory, this introduces an ambiguity. However, with $m(\eta) - (2m(\pi^\pm) + m(\pi^0)) = 164.7\,\mathrm{MeV}/c^2$, the decay $\eta \to \pi^+\pi^0\pi^-$ has very little phase space. This is visible in the left plot of figure 3.17, where the mass peak corresponding to the η is located at the lower end of the spectrum and as a result has very low "combinatorial" background. A continuation of the selection (that is, the case where an η candidate was found) contains to 1.9% events in which an ambiguity between two η candidates occurs.

Using the chosen π^-, the $(\pi^+\pi^-\pi^0)$ is fitted to the η mass. One might suspect that two independent fits acting on the same variables with different constraints might interfere with each other, that the compliance with the first fit hypothesis will be inadvertantly worsened by the second one. As can be seen in figure 3.18 by comparing the digamma-mass directly before and after this fit, the originally present π^0 peak only improves in quality, that is becomes narrower. This speaks in favour of the application of the fit and the selection of events.

The resulting final selection is $\eta\pi^-$, of which the mass spectrum is shown in the right half of figure 3.17. The spectrum is dominated by the $a_2(1320$.
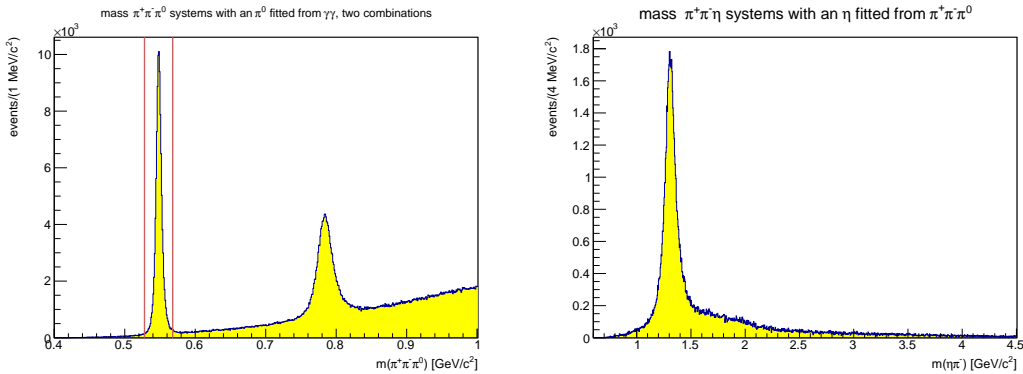

Fig. 3.17: Two relevant kinematic plots for the decay channel of $\eta\pi^- \to (\pi^+\pi^0\pi^-)\pi^-$. (left) The $(\pi^+\pi^-\pi^0)$ mass spectrum, filled for each of the two available combinations. The η mass window is marked. (right) The $(\eta\pi^-)$ mass spectrum for the final selection.
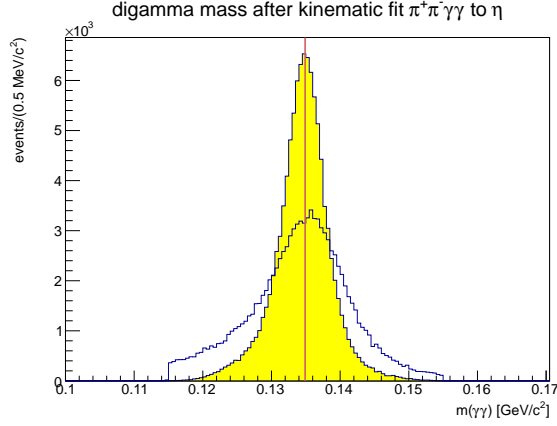
Fig. 3.18: The digamma mass spectrum is compared before and after a kinematic fit of a $(\pi^+\pi^-\gamma\gamma)$ within an η mass window to the η mass, where the $\gamma\gamma$ was also previously selected as a π^0 candidate.

3.4.2 Second stage, channel $\eta'\pi^- \to (\pi^+\pi^-\eta)\pi^-$

Methodically, this channel is very similar to the previous, only replacing $\pi^0 \to \eta$ and $\eta \to \eta'$. In fact, the mass window for η' candidates is $|m(\pi^+\pi^-\eta) - m(\eta')| < 20\,\mathrm{MeV}/c^2$ with the same width as that for η candidates. The requirement that such an η' candidate exists in the event then reduces the events to 5.9%. Similarly, the small phase space of the decay $\eta' \to \pi^+\pi^-\eta$ with $m(\eta') - 2m(\pi) - m(\eta) = 130.7\,\mathrm{MeV}/c^2$ results in ambiguous η' candidates for only 0.18% of the events where an η' candidate exists at all. Again,
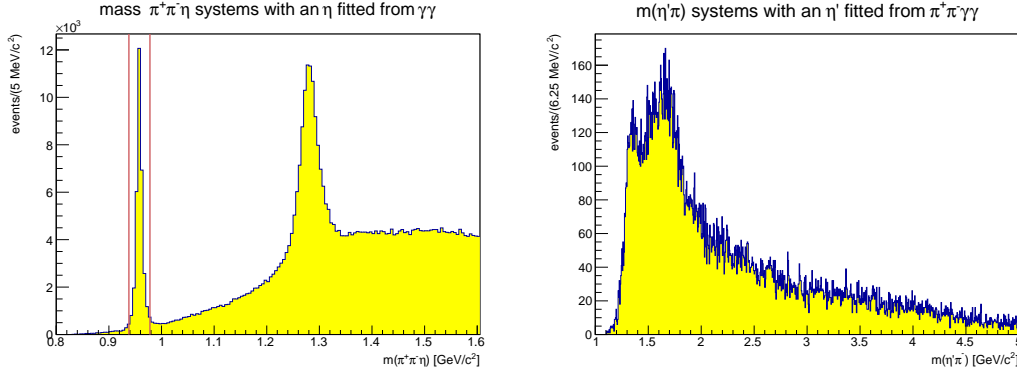

Fig. 3.19: Relevant kinematic plots for the decay channel of $\eta'\pi^- \to (\pi^+\eta\pi^-)\pi^-$. (left) The $\pi^+\pi^-\eta)$ mass spectrum, filled for each of the two available combinations. (right) The $(\eta'\pi^-)$ mass spectrum for the final selection. The used mass window is marked in the left plot.

the figure 3.20 shows a comparison showing that the π^0 peak in the $\gamma\gamma$ mass spectrum does not suffer from the kinematic fit where the digamma mass is left free.

The main difference lies in the mass spectrum of the $\eta'\pi^-$ final state, which is shown on the right side of figure 3.19. Instead of dominating the spectrum, the $a_2(1320)$ appears on the rising edge around $1.3\,\mathrm{GeV}/c^2$.
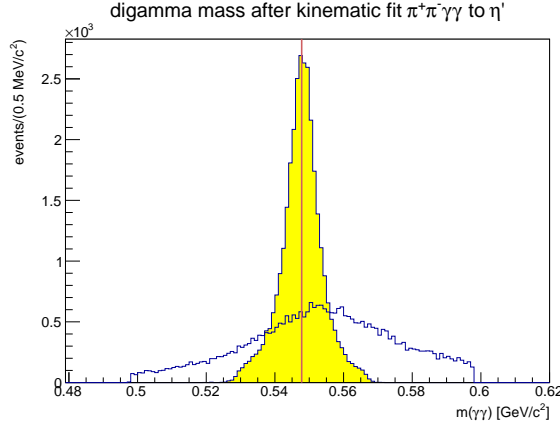

Fig. 3.20: The η peak in the digamma mass spectrum is improved by a kinematic fit of the $(\pi^+\pi^-\gamma\gamma)$ system to the η' mass, provided it lies in an η' mass window.

3.4.3 Second stage, channel $\eta'\pi^- \to (\pi^+\pi^-\eta(\to \pi^+\pi^0\pi^-))\pi^-$

The final state $\eta'\pi^-$ will be reconstructed from 3 π^-, $2\pi^+$ and a π^0 fitted from 2 γ. These are required to contain a candidate for the decay $\eta \to \pi^+\pi^0\pi^-$ and one for the decay $\eta' \to \pi^+\eta\pi^-$, where η is the same candidate found before.

Due to the large number of particle tracks, both these candidates have several combinations: There are $\binom{2}{1}\binom{3}{1} = 6$ $\pi^+\pi^0\pi^-$ combinations to be checked for η candidates, and $\binom{2}{2}\binom{3}{2} = 3$ $\pi^+\pi^-\eta$ which could be considered for η' candidates. Once any η candidate is chosen, one of these potential η' candidates can be excluded. For illustration, please refer to figure 3.23.

All six combinations of positive and negative pion are checked. Consequently, the mass spectrum of the $(\pi^+\pi^-\pi^0)$ system filled in each of these combinations shows a larger combinatorial background than the analogous plot in the first channel, where only the two possible combinations entered the plot. Similarly as in the previous channels, one η candidate with $\left|m(\pi^+\pi^-\pi^0) - m(\eta)\right| < 20\,\mathrm{MeV}/c^2$ is chosen, if it exists (for 13.4% of events). Using this η candidate, the mass spectrum for each of the remaining two π^- completing to a $(\pi^+\pi^-\eta((\pi^+\pi^-\pi^0)))$ combination is filled. If the mentioned η candidate *were* now fitted to the η mass as was done in the case of three charged pions, the effect would be adverse on the continued reconstruction of the η'. In order see this, we need to consider the background under the η. As mentioned before, this background is larger than in the other channels. If a background event were fitted to the η mass, its lack of connection to a physical η would mean that the cluster energies could be corrected *away* from the true values, or in other words, the π^0 peak would increase in width. This

increase in width would translate itself into the η' candidate spectrum, leading in the end to a larger background in the final selection.

One of these combinations which is also in the mass window of $|m(\pi^+\pi^-\eta) - m(\eta')| < 20\,\mathrm{MeV}/c^2$ is considered the final η' candidate. It exists for 0.74% of the events initially considered in this decay channel. This η' candidate, or rather the photon clusters in it, are then kinematically fitted. The constraint of this fit ensures both that $m(2\pi^+2\pi^-2\gamma) = m(\eta')$ and that $m(\gamma\gamma) = m(\pi^0)$. In contrast to the previously considered decay channels, the unconstrained system is the intermediary $(\pi^+\pi^-\pi^0)$. The figure 3.22 shows how the procedure still improves the mass peak.

The methodical risk of this process is that an event may contain more than one η candidates, some within an η' candidate and some not. In this case, the failure to consider each possiblity independently and resolve ambiguities when they arise opens up the possibility that this event would be discarded, simply because an η not within an η' was chosen. When the occurrences of this critical case are counted, however, it turns out it makes up for only 1.1% of those cases which lead to a selection at all. A larger problem seems to be the distinction between up to four equivalent η candidates which lead to an η' candidadate. However, since the ratio between the number of events with exactly one η' candidate over the number with ambiguous η' candidates is 25.8, the counted η candidates are likely belong to the same or no η' candidate instead of several, which would lead to ambiguities in the final selection.

This whole discussion is somewhat academical as the decay channel was not used for partial-wave analysis. Due to five charged pions and the longer decay chain, this decay
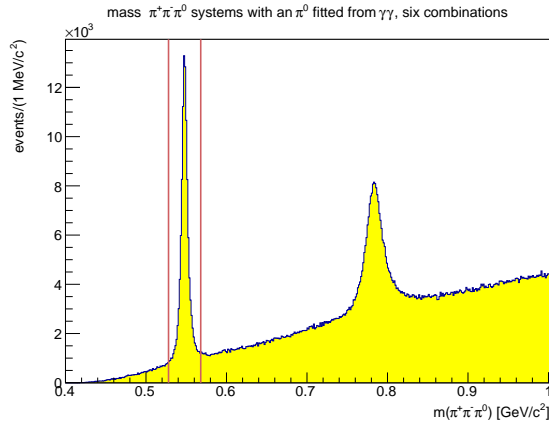

Fig. 3.21: The $(\pi^+\pi^-\pi^0)$ mass spectrum for each of the six combinations available. The η appears around $0.55\,\mathrm{GeV}/c^2$ alongside the $\omega(782)$ around $0.78\,\mathrm{GeV}/c^2$. Due to the greater number of combinations, the background is larger than in the same spectrum in the first channel. The mass range for η candidates is marked.

channel has far fewer events in the final selection than the other channels. The selection is not used for partial-wave analysis.
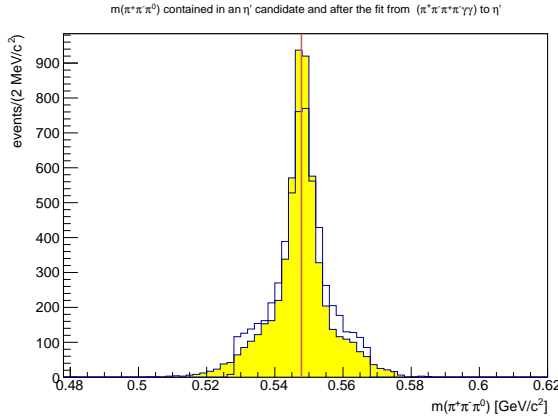
Fig. 3.22: Shown is the η peak in a selection of η candidates which are part of an η' candidate. In the yellow histogram, a kinematic fit is applied that uses two constraints; one on the mass of the $\gamma\gamma$ which appears in the η candidate to the π^0 mass; and one constraining the η' candidate formed with this η candidate and two additional charged pions to the η' mass. We observe that the peak becomes slightly narrower and spreads itself out along the eges. This figure plays a similar role as figure 3.20 and figure 3.18; only it shows that a third constraint would not be a good idea.
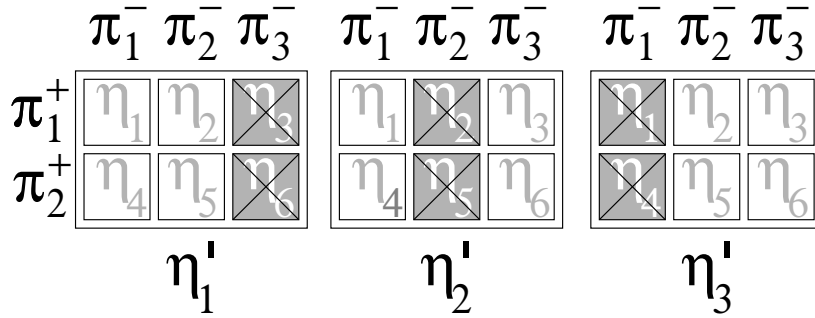

Fig. 3.23: The combinatorics in the five-track channel. Each box is one of three potential η' candidates, containing four of six potential η candidates constructed with combinations of one of three π^- and one of two π^+.
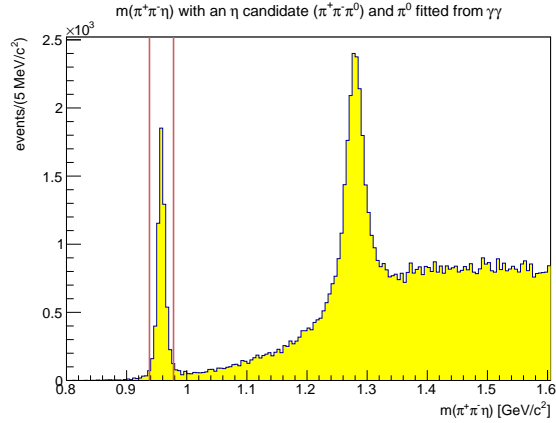
Fig. 3.24: The mass spectrum of $(\pi^+\pi^-\eta(\pi^+\pi^-\pi^0))$, where $\eta(\pi^+\pi^-\pi^0)$ is an unfitted system within the η mass range. The peaks of η' and $f_1(1285)$ appear as in the previous channel, but with lower statistics. The mass range for η' candidates is marked.

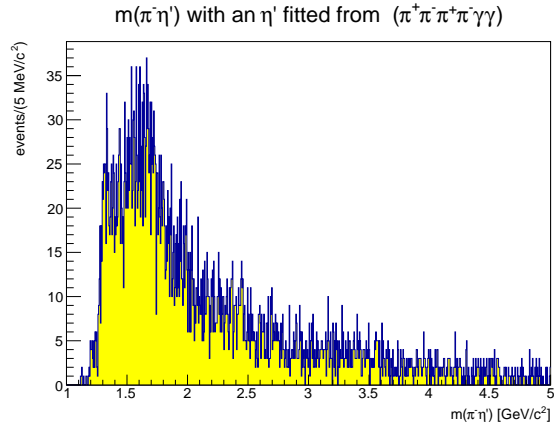Fig. 3.25: The mass spectrum for the final selection of the $\eta'\pi^-$ state shows a hint of the $a_2(1320)$ at low masses around $1.2\,\text{GeV}$, although the available statistics are not sufficient to confirm its existence in this mass spectrum.

29

3.5 Conclusions

The starting point of the selection was the 2008 hadron run of COMPASS. It consists of $6.01 \cdot 10^9$ events. The results of the selection are three data samples, measuring 110 806 events for the $\eta\pi^-$ state, 3 4379 events for the $\eta' \to \pi^+\pi^-\gamma\gamma$ and 6 052 events for $\eta' \to 4\pi^\pm\gamma\gamma$ decay channel.

The BNL experiment E852 studied the reaction $\pi^- + p \to \eta'\pi^- p$ [3]. They obtained a sample consisting of 5765 events, using the decays $\eta' \to \pi^+\pi^-\eta$ and $\eta \to \gamma\gamma$. The very same decay channel is an important part of the presented selection of the $\eta'\pi^-$ final state. However, the final selection COMPASS data arrived at an almost six times larger sample fitting the same signature. Prima facie, this puts the COMPASS analysis to follow the selection at an advantage. We are going to compare a mass distribution from the 2008 preprint with the equivalent one from this analysis in figures 3.26 and 3.27. The same plots can also be found in section 3.4.
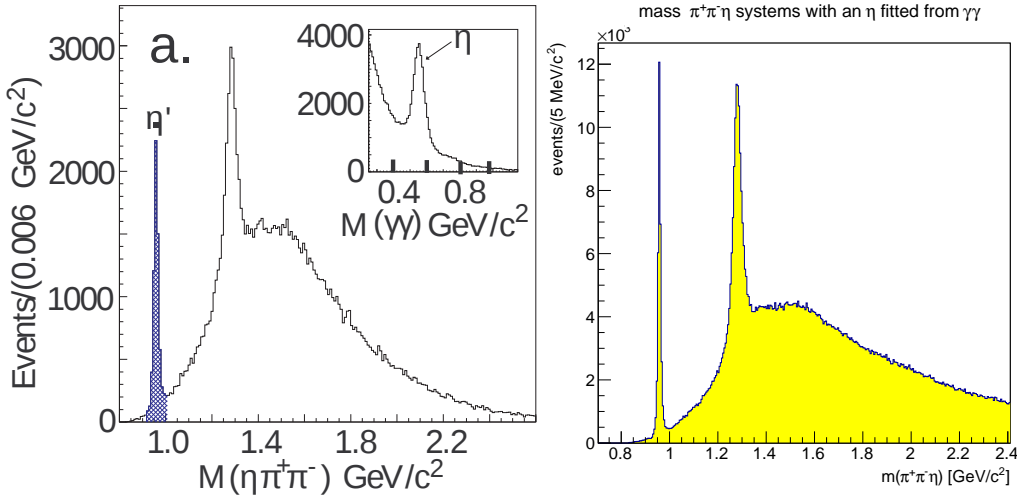

Fig. 3.26: The $\pi^+\pi^-\eta$ mass distribution, to the left from E852, to the right from COMPASS. The $f_1(1285)$ clearly appears on a larger background in the E852 plot.

The same E852 experiment also studied the $\eta\pi^-$ final state [2], although in the decay channel $\eta \to \gamma\gamma$, which was not considered for this analysis. There, they show the invariant mass spectrum of $\eta\pi^-$, which also lends itself to a comparison; therefore, it is shown alongside the equivalent plot from this analysis in figure 3.28.

As mentioned in the introduction, a similar analysis and crosscheck was performed earlier by Tobias Schlüter and Hauke Wöhrmann. They arrived at a larger sample of the final states. Apart from optimizing minor aspects, several opportunities remain to improve the selection, gaining a larger sample and a smaller background.

- For once, many decay channels of the final states remained unconsidered. Tackling the difficulties with these channels would need to be weighed against the relative statistical benefit.
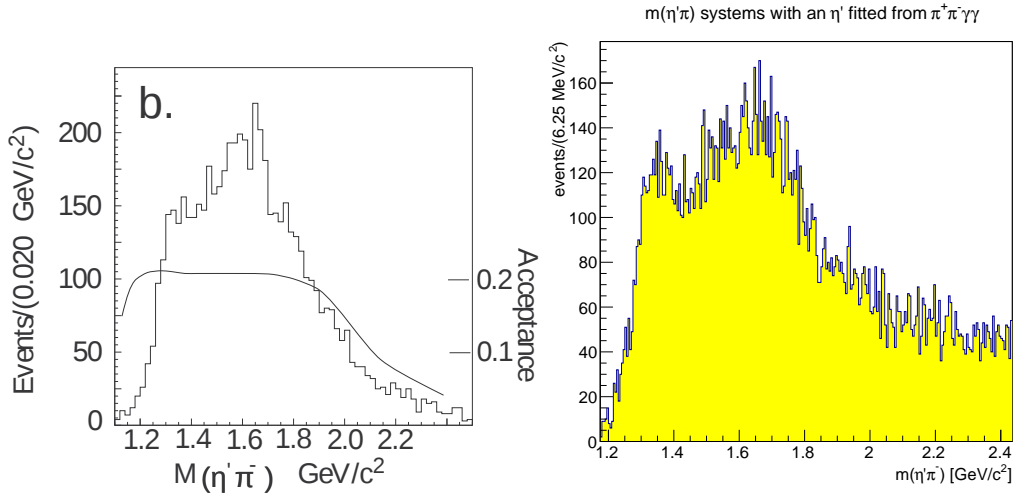
Fig. 3.27: The $\pi^-\eta'$ mass distribution, to the left from E852, to the right from COM-
PASS. The $a_2(1320)$ appears more distinguished in the COMPASS plot. The
mass distribution also does not suffer from the breakdown of acceptance at
$2\,\text{GeV}/c^2$ that is indicated in the E852 plot.

- A further opportunity is the final state $f_1(1285)\pi^-$. In each $m(\pi^+\pi^-\eta)$ spectrum, the $f_1(1285)$ appeared alongside the $\eta'(958)$. Therefore, the existing selection might be put to use taking in another final state.

- Then, the possibility for a third exclusivity cut remains, for example on the magnitude of transverse momenta instead of merely their direction (see section 3.3.2).

- The slight incongruence between the photon selection in the first and second stage (see section 3.3.2) is sub-optimal as some photons are lost this way.

- In the final selections, a better treatment of ambiguities could be implemented.

- Also, it would be interesting to study the effect the values of the photon energy thresholds have (see section 3.3.1), ultimately finding an optimal set of energy thresholds for the particular analysis performed.

- Finally, the photon reconstruction efficiency could be improved upon by taking events where the photon converts ($\gamma \to e^+e^-$) in a nuclear field into account using tracking detectors and electromagnetic calorimeters.

3.6 Noted issues

Alternative charges

In the mDSTs, two different methods can be called to report the charge associated with a particle track: For "particle" the reference to an object of the class PaParticle,
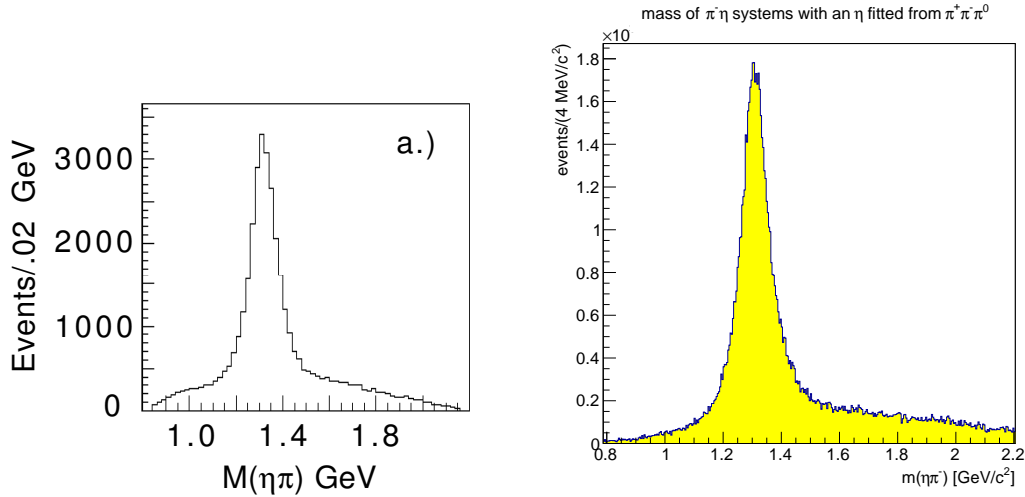
Fig. 3.28: The $\pi^-\eta'$ mass distribution, to the left from E852, to the right from COM-
PASS. The $a_2(1320)$ dominates both distributions. Even though the two dis-
tributions result from two different decay channels, the only overtly apparent
difference is a slightly smaller peak to background ratio in the E852 plot.

belonging to the particles associated as exiting from the primary vertex "pv" with the in-
dex "iv", the charge can be obtained as Q=particle.Q() or Q'=particle.ParInVtx(iv).Q().
The possibility of a difference between the two made itself apparent when we found that
our cuts on charge conservation used either method respectively and thus differed.

The first method is the result of a fit on the bending radius of its trajectory in a
spectrometer magnet, which results in a momentum and charge sign (with the absolute
value of the charge predetermined as 1). After the fit on the particle track is complete,
a primary vertex common to all tracks can be reconstructed. Once this is done, a
second fit is performed involving the new vertex as a point in the trajectory. For high
momenta, that is straight trajectories, this can flip the sign of the charge. Statistically,
the incongruence creates a mismatch for only 0.01% of the charges entering into the
statistic.

ECAL1 offset

In the production of the analyzed 2008 data, a z-position corresponding to the mid-
point of the ECAL1 calorimeter of 1412.5 cm was used. As was later discovered, this
represented a shift of 13 cm versus the actual position. In order to obtain correct kine-
matical data from calorimeter clusters in ECAL1, the calculation of four-momenta in-
corporated a shift in the opposite direction ($z \rightarrow z - 13$ cm) in order to compensate
the error. The magnitude of the effect can be seen in the position of the π^0 peak in
the digamma mass spectrum, which is $0.135 \, \text{GeV}/c^2$ before and $0.136 \, \text{GeV}/c^2$ after the
correction. The influence of this error is of course alleviated by the clusters in ECAL2,
which make up over half (57%) of the recorded photon-like clusters.

Radial calorimeter cell search

A bug in the PaCaloClus::iCell() method responsible for finding a cell number corresponding to (x, y) coordinates led to segementation errors when applying the calibration to clusters from different calorimeters. The method uses a lookup table of radii for various cells in order minimize the number of checked cells when the cell index for a certain $x - y$ position needs to be found by exploiting the fact that the density of clusters decreases outwards. Tobias Schlüter discovered the error to stem from an incorrect initialisation of the mentioned lookup table, which resulted in a table specific to one calorimeter being used for the other.

Chapter 4

Acknowledgements

I would like to thank Professor Stephan Paul of the chair E18 for supplying me with the subject of this thesis and agreeing to give the work the nature of a cross-check. This had the effect of bringing me into close contact with actually ongoing analysis and a wealth of knowledge and experience in the form of Tobias Schlüter. Thanks go to him for putting up with my questions and misguided efforts, supporting me in making all the relevant deadlines, and discovering an uncounted number of bugs, both in my code, in a Phast library, and those in his own which I failed to notice, using his superior programming skills. Further than that, without his methods of cluster calibration and constrained fitting, this thesis would have significantly less to talk about, and without his gHist library I would have been hestitant to add many plots which later might have turned out to be meaningful. No little amount of praise is due to Florian Haas for getting me started very quickly from the point of having no experience in C++, ROOT or Phast to using all three and guiding me through the final phase of concentrating all those weeks spent hacking away at user event functions into a thesis of 34 pages. Boris Grube also gave far too much of his time, being readily available for many technical problems and stylistic guidance. Stefan Pflüger showed me the use of several helper libraries and Sebastian Uhl provided the LaTeX template on which the style of this thesis is based.

Bibliography

[1] J. N. Hedditch *et al.* "1^+ exotic meson at light quark masses". Phys. Rev. D72 (2005) 114507.

[2] E852 Collaboration, D. Thompson *et al.*, Evidence for Exotic Meson Production in the Reaction $\pi^- p \to \eta \pi^- p$ at 18 GeV/c, Phys. Rev. Lett. **79** (1997) 16301633, arXiv:hep-ex/9705011.

[3] E852 Collaboration, E. I. Ivanov et al., Observation of exotic meson production in the reaction $\pi^- p \to \eta' \pi^- p$ at 18 GeV/c, Phys. Rev. Lett. 86 (2001) 39773980, arXiv:hep-ex/0101058.

[4] Tobias Schlüter, "A code for kinematic fitting with constraints from intermediate particle masses", COMPASS note 2007-10

[5] Tobias Schlüter, "Overview of neutral hadron channel analysis", COMPASS Collaboration meeting, March 2010

[6] L. Gatignon, M. Leberig *et al.*, "The M2 Beam Line"

[7] COMPASS Collaboration, P. Abbon et al., "The COMPASS Experiment at CERN", Nucl. Instr. and Meth. A 577 (2007) 455518, arXiv:hep-ex/0703049

[8] Tobias Schlüter *et al.*, "Partial-wave analysis of 2008 $\eta' \pi^-$ data" - release discussion at the COMPASS Analysis Meeting on June 2nd, 2011.